

The Role of Phosphate Functionalization on the Oxygen Evolution Reaction Activity of Cobalt-Based Oxides at Different pH Values

Wataru Yoshimune, Juliana B. Falqueto, Adam H. Clark, Nur Sena Yüzbası, Thomas Graule, Dominika Baster, Mario El Kazzi, Thomas J. Schmidt, and Emiliana Fabbri*

Cobalt-based oxides have attracted attention as active electrocatalysts for the oxygen evolution reaction (OER) in alkaline electrolytes. However, highly OER active catalysts at near-neutral pHs are also desired for practical applications. Herein, a dry phosphate functionalization process is presented to enhance the OER activity of different cobalt-based catalysts at near-neutral pHs. Electrochemical evaluations show that the P-functionalization can effectively improve the OER activity at near-neutral pHs for $\text{La}_{0.2}\text{Sr}_{0.8}\text{CoO}_{3-\delta}$, $\text{La}_{0.2}\text{Sr}_{0.8}\text{Co}_{0.8}\text{Fe}_{0.2}\text{O}_{3-\delta}$, and CoO_x catalysts, but not for $\text{La}_{0.5}\text{Sr}_{1.5}\text{CoO}_{4-\delta}$. Bulk and surface sensitive X-ray absorption spectroscopy and X-ray photoelectron spectroscopy unveil the influence of P incorporated in the order of ppm on the electronic state, local structure, and surface composition of the investigated catalysts. The P-functionalization reduces the Co oxidation state in $\text{La}_{0.2}\text{Sr}_{0.8}\text{CoO}_{3-\delta}$ and $\text{La}_{0.5}\text{Sr}_{1.5}\text{CoO}_{4-\delta}$, but the latter also presents significant Sr-based segregations on the surface-inhibiting OER activity at near-neutral pHs. Differently, $\text{La}_{0.2}\text{Sr}_{0.8}\text{CoO}_{3-\delta}$ and to a lesser extent $\text{La}_{0.2}\text{Sr}_{0.8}\text{Co}_{0.8}\text{Fe}_{0.2}\text{O}_{3-\delta}$ and CoO_x shows improved OER activity at neutral pH after the P-functionalization. The findings disclose that P-functionalization successfully enhances OER activity at near-neutral pHs and that both phosphate ion assistance in the OER mechanism and catalyst Co oxidation state can play a role in the enhanced OER activity.

especially for future automobiles equipped with polymer electrolyte fuel cells or hydrogen-powered engines.^[1] Market expansion requires large-scale hydrogen production facilities, and proton exchange membrane water electrolysis (PEMWE) is one promising production system. However, strong acids used as the electrolyte and membrane in PEMWE cells corrode metal oxides, requiring acid-tolerant precious metals (e.g., Pt, RuO_2 , and IrO_2). In alkaline exchange membrane water electrolysis (AEMWE), various non-precious metal oxides function as anode catalysts, potentially overcoming the problem of cost reduction.^[2]

Perovskite oxides such as ABO_3 single perovskites,^[3] $\text{AA}'\text{B}_2\text{O}_6$ or $\text{A}_2\text{BB}'\text{O}_6$ double perovskites,^[4] $\text{AB}_3\text{B}'_4\text{O}_{12}$ quadruple perovskites,^[5] $\text{A}_{n+1}\text{B}_n\text{O}_{3n+1}$ Ruddlesden–Popper (RP) perovskites,^[6] and $\text{A}_2\text{B}_2\text{O}_5$ brownmillerites^[7] have been suggested as promising oxygen evolution reaction (OER) catalysts in alkaline electrolytes. The rigid perovskite framework permits the substitution of cations with other cation elements, e.g.,

$(\text{A}_x\text{A}'_{1-x})(\text{B}_y\text{B}'_{1-y})\text{O}_{3-\delta}$ in ABO_3 perovskites. The wide selection possibilities in the chemical composition expand the exploration for highly active OER catalysts. Within the broad perovskite family, $\text{Ba}_{0.5}\text{Sr}_{0.5}\text{Co}_{0.8}\text{Fe}_{0.2}\text{O}_{3-\delta}$ ^[8] and $\text{La}_{0.2}\text{Sr}_{0.8}\text{Co}_{0.8}\text{Fe}_{0.2}\text{O}_{3-\delta}$ ^[8,9]


1. Introduction

Green energy is progressively replacing fossil fuels toward a sustainable energy system. Hydrogen is an attractive energy vector,

W. Yoshimune, J. B. Falqueto, A. H. Clark, D. Baster, M. El Kazzi, T. J. Schmidt, E. Fabbri
Energy and Environment Research Division
Paul Scherrer Institut PSI
CH-5232 Villigen, Switzerland
E-mail: emiliana.fabbri@psi.ch

N. S. Yüzbası, T. Graule
Laboratory for High Performance Ceramics
Empa, Swiss Federal Laboratories for Materials Science and Technology
CH-8600 Dübendorf, Switzerland

T. J. Schmidt
Laboratory of Physical Chemistry
ETH Zurich
CH-8093 Zürich, Switzerland

 The ORCID identification number(s) for the author(s) of this article can be found under <https://doi.org/10.1002/ssstr.202300106>.

© 2023 The Authors. Small Structures published by Wiley-VCH GmbH. This is an open access article under the terms of the Creative Commons Attribution License, which permits use, distribution and reproduction in any medium, provided the original work is properly cited.

DOI: 10.1002/ssstr.202300106

have been identified as two of the most active perovskite catalysts for AEMWE applications.

The OER mechanism on an oxide catalyst surface has been long assumed to proceed solely by four successive proton-coupled electron transfer (PCET) steps, where the surface metal cation M^{n+} sites are the active site.^[2] However, the lattice oxygen evolution reaction (LOER) has been proposed recently as an alternative mechanism in the alkaline water splitting particularly for perovskite catalysts, which proceeds through the involvement of lattice oxygen atoms.^[10] Indeed, both theoretical calculations and in situ ^{18}O isotope labeling mass spectrometry experimental evidence suggest that LOER is the preferential oxygen evolution mechanism for many active perovskite catalysts.^[10]

Figure 1 describes a possible LOER mechanism on the surface of perovskite oxides. As illustrated in Figure 1, superficial O^{2-} sites can be considered the active sites for OH^- adsorption in the LOER. OH^- ions attack the constructed $\text{M}-\text{O}(\text{OH})$ layer, forming the intermediate $\text{M}-\text{O}(\text{O}^*)$ phase. The intermediate phase releases O_2 by creating oxygen vacancies (\bullet). Subsequently, OH^- ions from the electrolyte compensate for the oxygen vacancies. Alternatively, the created oxygen vacancies promote surface cation dissolution. Lopes et al. revealed that oxygen vacancies in $\text{La}_{1-x}\text{Sr}_x\text{CoO}_{3-\delta}$ contributed to faster A-site dissolution and perovskite surface conversion into a highly active oxyhydroxide $\text{CoO}(\text{OH})$ layer in an alkaline electrolyte.^[11] *Operando* X-ray absorption spectroscopy (XAS) measurements confirmed the formation of a highly active self-assembled $(\text{Co}/\text{Fe})\text{O}(\text{OH})$ phase on the surface of $\text{Ba}_{0.5}\text{Sr}_{0.5}\text{Co}_{0.8}\text{Fe}_{0.2}\text{O}_{3-\delta}$, as a result of LOER and metal dissolution led to forming a porous amorphous oxyhydroxide $\text{M}-\text{O}(\text{OH})$ layer with a high surface area, providing good stability under

a dynamic equilibrium between cation dissolution and redeposition.^[8e,11]

Perovskite oxide catalysts can exhibit relatively high OER activity and stability at high basicity ($>\text{pH } 13$), but their electrochemical properties degrade in near-neutral pH (7–10) environments.^[12] Considering the proton transfer that assists the deprotonation step from $\text{M}-\text{O}(\text{OH})$ to $\text{M}-\text{O}(\text{O}^*)$ on the active site as the rate-determining step in LOER (Figure 1),^[10c] a variation in the OH^- concentration to near-neutral pHs would result in a significant decrease in the OER activity. However, near-neutral pHs are highly relevant in practical applications. Using KOH electrolytes in AEMWE creates vulnerability to carbonation during operation, lowering the initially high pH level toward near-neutral pHs.^[13] Carbonation is a significant problem in recently established AEMWE systems using a carbonate membrane that operates as a coelectrolysis cell by replacing the cathodic hydrogen evolution reaction with carbon oxide reduction.^[14] Yang et al. proposed a strategy using “phosphate ion functionalization” to enhance the OER activity at near-neutral pH by promoting interfacial proton transfer.^[15] The authors claim that phosphate groups have a pK_a (12.67) lower than the pH of the electrolyte and are stable under typical AEMWE operating conditions, and, thus, they could effectively improve interfacial proton transfer at quasi-neutral pHs in the LOER.

In this study, we have examined the impact of phosphate functionalization on the OER activity of several cobalt-based oxides at different pHs. We employed $\text{La}_{0.2}\text{Sr}_{0.8}\text{CoO}_{3-\delta}$ (LSC) and $\text{La}_{0.2}\text{Sr}_{0.8}\text{Co}_{0.8}\text{Fe}_{0.2}\text{O}_{3-\delta}$ (LSCF) as ABO_3 perovskites, $\text{La}_{0.5}\text{Sr}_{1.5}\text{CoO}_{4-\delta}$ (RP-LSC) as RP perovskites, and CoO_x as binary cobalt oxides containing rock salt CoO and spinel Co_3O_4 (see the crystal structures in **Figure 2** drawn by using the VESTA software^[16]). LSC is a promising material as OER catalyst, and a previous study showed that phosphate-functionalized LSC has relatively high OER activity in a wide alkaline pH range.^[15] LSCF incorporates Fe on the B sites of LSC, as it is well known that Fe substitution on the Co site increases the OER activity at pH 13.^[8g,12b] RP-LSC is classified as the same perovskite family as LSC, but with a layered K_2NiF_4 structure. Both LSC and RP-LSC easily display surface segregation of Sr (or related compounds) to different degrees.^[17] Finally, CoO_x has been chosen as a reference material because it is one of the most common and relatively active OER catalyst. All oxide catalysts were prepared by

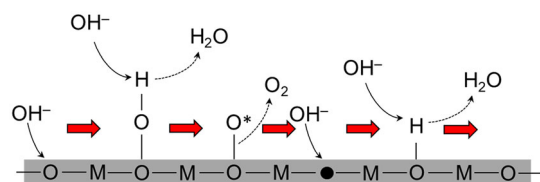


Figure 1. LOER mechanism in an alkaline electrolyte on the surface of perovskite oxides. A black circle (\bullet) indicates an oxygen vacancy.

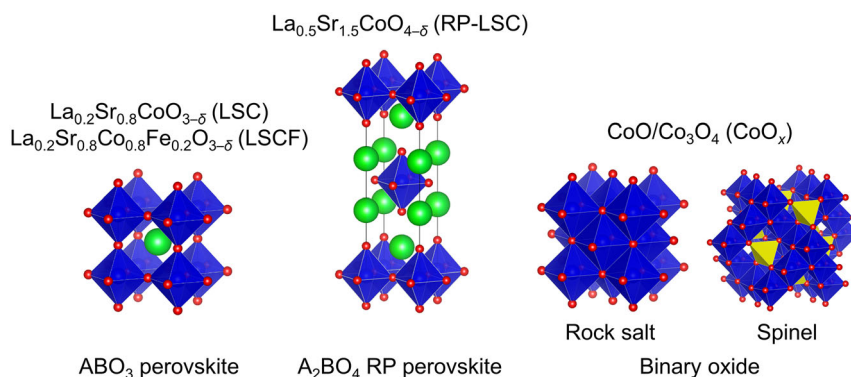


Figure 2. Crystal structure of cobalt-based oxides. ABO_3 single and A_2B_4 RP types were used as perovskite oxides. Binary cobalt oxide labeled as CoO_x contains rock salt CoO and spinel Co_3O_4 .

the flame spray synthesis method^[8e,g,h,12b] and characterized by X-ray diffraction (XRD), X-ray photoelectron spectroscopy (XPS), and soft and hard XAS. The electrocatalytic activity toward OER of the different nanoparticle catalysts was investigated in electrolytes with different pH values (pH = 7, 12.5, 13, and 13.5) and correlated with the observed modification induced by the phosphate functionalization.

2. Results and Discussion

Our previous studies showed that the flame spray synthesis method yields nanoparticles of LSC, LSCF, and CoO in the range of 10–30 nm with a higher surface area (over 5 times) than particles synthesized by the widely used sol-gel method, ranging between 20 and 45 m² g⁻¹.^[8e] Figure 3 shows XRD patterns of LSC, LSCF, RP-LSC, and CoO_x. In all as-synthesized samples, an almost pure main phase marked by (○) was achieved with secondary phases marked by (□/■). In LSC and RP-LSC, small amounts of metal carbonates were observed as impurities, while in CoO_x, CoO, and Co₃O₄ appeared as the primary and secondary phases, respectively. LSC and LSCF had a cubic perovskite phase, with LSCF exhibiting a slightly larger lattice constant than LSC (3.87 Å for LSC and 3.89 Å for LSCF).

As-synthesized LSC nanoparticles were initially treated for phosphate ion functionalization using a wet process,^[15] described in details in the method section. After the phosphate ion functionalization wet process, the catalyst powder was significantly more agglomerated than the pristine one (see Figure S1a, Supporting Information) and the change in morphology negatively impacted the OER activity. Figure S1b,c, Supporting Information, shows CVs and Tafel plots for as-synthesized

and wet-treated powder samples, respectively. As shown in the inset of Figure S1b, Supporting Information, the capacitive current was reduced in the wet-treated sample compared to the as-synthesized sample. The decrease in capacitive current can be explained by the agglomeration of the nanoparticles after the wet process, leading to a decrease of the catalyst surface area (see Figure S1a, Supporting Information). The wet treatment process led to a significant reduction in the mass activity for LSC; for example, in 0.1 M KOH and at 1.58 V_{RHE} a decrease of 40% in the mass current density and an increase in the Tafel slope from 51 to 84 mV dec⁻¹ can be observed. These results showed that the wet process is unsuitable for nanoparticle catalysts. Therefore, a dry process was successfully developed to avoid particle agglomeration for nanosized catalysts. In the developed dry P-functionalization process, the oxide catalysts are reduced by PH₃ gas from the thermal decomposition of NaH₂PO₂ and simultaneously covered with H₃PO₄ (e.g., an ABO₃ perovskite oxides reacts as follows: ABO₃ + xPH₃ → ABO_{3-4x} + xH₃PO₄).^[18a] No major agglomeration was observed after the dry phosphate treatment (Figure S1a, Supporting Information). We confirmed no difference in the OER activity before and after heat treatment without P sources (Figure S2, Supporting Information). The results show that the dry P-functionalization process at relatively low temperatures (≈300 °C) does not affect the particle size of nanosized catalysts. Therefore, the dry treatment was successfully used to functionalize all the catalysts of interest.

XRD patterns of phosphate-treated samples (pLSC, pLSCF, pRP-LSC, and pCoO_x) are displayed in Figure 3, along with those of as-synthesized samples. No metal phosphide impurity phase appeared in all samples after the phosphate treatment, but some minor secondary phases related to SrCO₃ and La₂(CO₃)₃

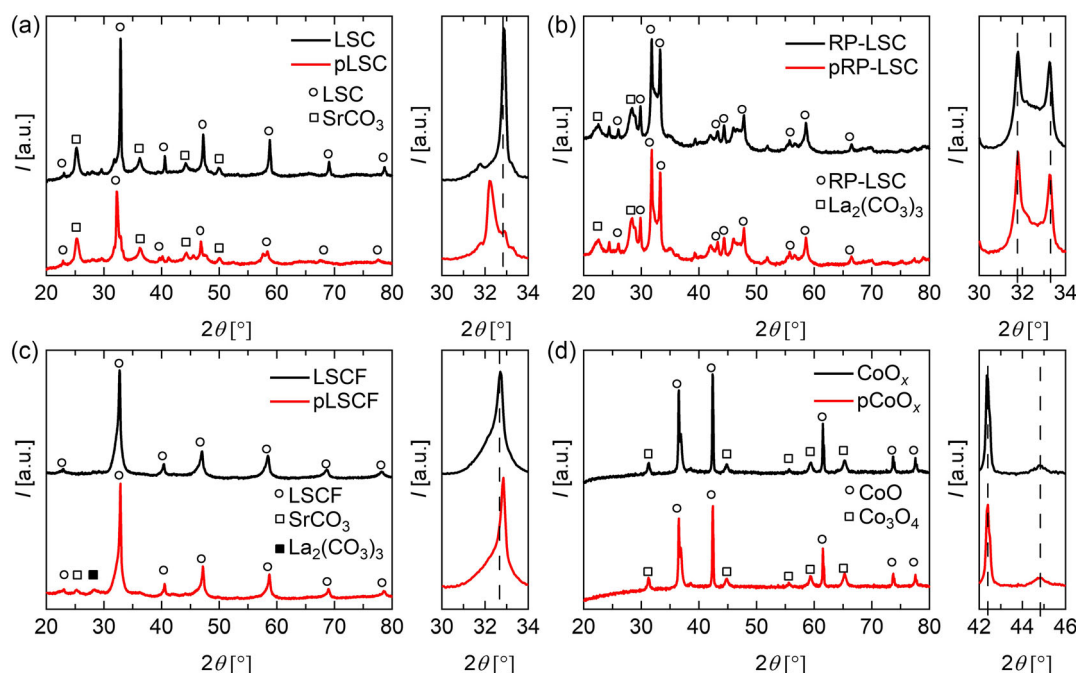


Figure 3. XRD patterns: a) LSC and pLSC; b) RP-LSC and pRP-LSC; c) LSCF and pLSCF; d) CoO_x and pCoO_x. pLSC, pLSCF, pRP-LSC, and pCoO_x represent phosphate-treated catalysts. The enlarged figures are placed on the right side to show the peak shift. The dashed lines indicate the guide to the eye for the peak shift.

appeared after the treatment for the LSCF sample. As shown in the enlarged images of Figure 3, a pronounced peak shift of more than 0.5° was observed only in LSC after the phosphate treatment. The lattice constants were assigned to be 3.87 \AA for LSC and 3.95 \AA for pLSC from the XRD patterns, indicating LSC was strongly reduced via phosphate treatment. RP-LSC and CoO_x showed no change in the lattice constants, while a slight increase in the lattice constants was observed for LSCF.

To investigate the amount of P incorporated on the surface of the treated catalyst samples, inductively coupled plasma optical emission spectrometer (ICP-OES) analysis was carried out. The concentration of P in the pCoO_x reaches 49 ppm, while for pLSC, pLSCF, and pRP-LSC perovskites the amount of incorporated P is about 3, 10, and 6 ppm, respectively, confirming that a tiny amount of P was incorporated into the catalyst surface. Interestingly, even though the samples underwent the same P-functionalization process, different amount of P could be incorporated on the surface of CoO_x compared to the perovskite structures. Phosphorus bands collected for the phosphate-treated catalysts and calibration curve of P standard solutions are reported in Figure S3, Supporting Information.

XAS measurements were performed at the Co K-edge to investigate the bulk Co valence state for all catalysts. The Co K-edge X-ray absorption near-edge spectroscopy (XANES) profiles (Figure 4a–f) show that the Co valence state in all investigated samples is between +2 and +3, as read from a comparison of the relative energy positions of the sample profiles and the standards (LaCoO_3 labeled as LCO and CoO). The Co valence states of the investigated samples were estimated from the energy position of the normalized absorption edge at $\mu = 0.5$ (considering the standards CoO and LCO with Co atoms in 2+ and 3+ state, respectively) and they are summarized in Figure 4g. CoO_x showed the most reduced Co valence state in the as-synthesized catalysts (around +2.25), while the other catalysts presented a Co

valence state between +2.5 and +2.9. The XANES profiles indicated a clear trend toward a lower oxidation state (shift in the Co K-edge toward lower energy at the same normalized intensity) in LSC and RP-LSC after the phosphate treatment, while only minor changes (toward an increase of Co oxidation state) were observed at the Co K-edge for LSCF and CoO_x . It must be noted that pLSCF showed an increase of secondary phases compared to LSCF (see Figure 3c). The Fe K-edge XANES profiles of LSCF and pLSCF (Figure S4, Supporting Information) indicate that Fe valence state was almost the same before and after the phosphate treatment.

Figure 5 displays the surface-sensitive Co L-edge soft XAS spectra recorded in total electron-yield (TEY) mode. Changes in the peak positions and relative intensity of LSC and RP-LSC with the phosphate treatment showed the same trend as the Co K-edge XANES profiles. The peak shift indicates that LSC and RP-LSC have reduced Co valence states in the phosphate-treated samples both in the bulk and surface of the catalysts. Also, consistently with the Co K-edge XANES profiles, the soft XAS spectra recorded in TEY for CoO_x and LSCF show only minor changes. In addition, differences in peak intensity between cobalt-based oxides can be observed. XAS in TEY being a “surface-sensitive” measurement detects the number of cobalt atoms on the surface; thus the lower the Co L-edge peak intensity, the lower is the concentration of catalytic active Co atoms on the surface. The trend in the peak intensity follows the trend: $\text{CoO}_x > \text{LSC} \approx \text{LSCF} > \text{RP-LSC}$. The decrease in the Co L-edge peak most probably results from Sr-based surface segregation, particularly for the RP-LSC sample which displays the lowest Co L-edge peak intensity. Indeed, it is widely reported in the literature by performing XPS investigations that $\text{La}_{1-x}\text{Sr}_x\text{CoO}_{3-\delta}$ samples display SrO-based surface segregation.^[17a,b] For RP-LSC, the A_2BO_4 RP-type perovskite has an alternating ABO_3 framework and AO rock salt layer (see the crystal structure in

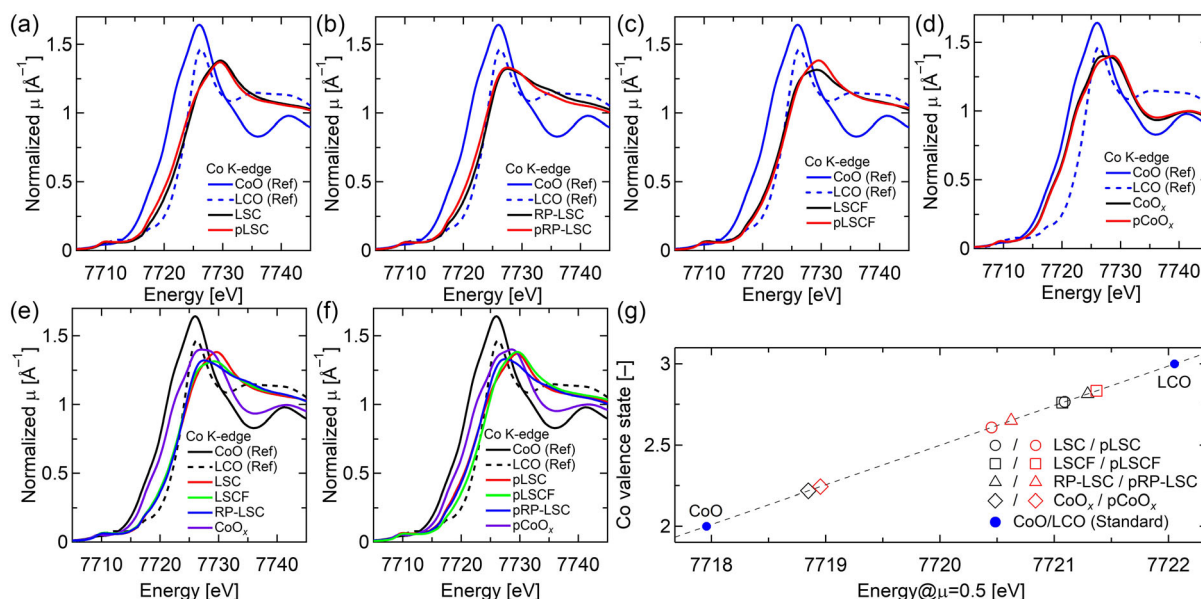


Figure 4. Co K-edge XANES profiles: a) LSC and pLSC; b) RP-LSC and pRP-LSC; c) LSCF and pLSCF; d) CoO_x and pCoO_x ; e) all as-synthesized samples; f) all phosphate-treated samples. g) Summary of Co oxidation states before and after the P-functionalization for all the investigated samples. CoO and LaCoO_3 (LCO) are standards for the comparison.

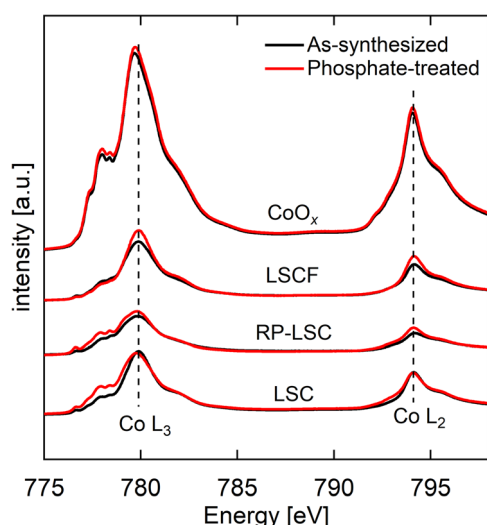


Figure 5. Co L-edge XAS profiles for all the investigated samples measured by soft XAS in TEY mode.

Figure 2) and the extra rock salt layer can cause even more surface segregation than in $\text{La}_{1-x}\text{Sr}_x\text{CoO}_{3-\delta}$.^[17c]

We have carried out XPS analysis to further investigate the surface of the as-prepared and modified samples. For pLSC, pRP-LSC, and pLSCF, the Sr 3d spectra (shown in Figure 6a) overlap with the P 2p_{3/2} core level (≈133.5 eV) and the La 4p_{3/2} core level falls in the same region as the P 2s core level, making the identification of the P 2p_{3/2} or 2s spectra for these samples not accurate. As shown in Figure S5, Supporting Information, small peaks attributed to P 2s and P 2p_{3/2} are actually visible in the XPS profile acquired on the pCoO_x sample (catalyst without Sr and La in the chemical composition) in agreement with the ICP-OES measurements.^[15] For all the investigated samples containing Sr, the Sr 3d spectrum presents several peaks, indicating that in addition to Sr in the lattice, Sr-based surface segregations are present. In addition, great differences in the Sr 3d peaks could be observed for some samples after the P-functionalization samples. The Sr 3d peak at lower binding energy (≈131.4 eV) is ascribed to lattice strontium

(Sr_{bulk}), while the peak at higher binding energy (≈133 eV) is associated to surface-segregated strontium (Sr_{surface}), which can be either SrCO₃ or SrO.^[17a] Sr_{surface} in LSC was invariant with the phosphate treatment, but it slightly increased in LSCF and it was greatly enhanced in RP-LSC after the phosphate treatment. Thus, for all the perovskite samples except for LSC, the aforementioned Sr-based surface modifications were enhanced by the P-treatment, inducing a stronger Sr-segregation on the surface. Figure 6b displays the Co 2p XPS profiles. The two peaks in the Co 2p XPS profiles derive from Co 2p_{3/2} at ≈780 eV and Co 2p_{1/2} at ≈795 eV.^[15] The peak intensity in RP-LSC was lower than that of the other catalysts. A decrease in the peak intensity denotes a decreased concentration of the catalytic active CoO₆ layer probably due to the presence of a SrO-based surface segregated layer on the surface of RP-LSC, in agreement with soft XAS (TEY) data.

Figure 7 displays CVs after 25 reverse scans, recorded between 1 V_{RHE} and 1.7 V_{RHE} at 10 mV s⁻¹ for as-synthesized and phosphate-treated catalysts at (a–d) pH 13 and (e–h) pH 7. Electrolytes with pH values of 13 and 7 were prepared using 0.1 M KOH and 0.1 M K₂HPO₄/KH₂PO₄ buffer, respectively. Between 1.2 V_{RHE} and 1.3 V_{RHE}, where capacitive currents dominate, the CV mostly overlapped each other. The results suggested that the surface area did not significantly change with the phosphate treatment. The inset of Figure 7a–d, related to CVs at pH 13, demonstrates that as-synthesized catalysts formed a stable quasi-reversible Co(III)/Co(II) redox couple at ≈1.1 V_{RHE}. After the phosphate treatment, this redox couple appears slightly suppressed for the perovskite samples, even though the perovskites present the lowest amount of P incorporated on the surface. At quasi-neutral pHs, the redox peak at ≈1.1 V_{RHE} is no more present for perovskites samples (as-prepared and P-functionalized), and the only observable redox couple is between ≈1.4 and 1.6 V_{RHE}. In the literature, a Co redox couple within ≈1.4–1.6 V_{RHE} potential range is generally assigned to Co(IV)/Co(III) transition when measured in alkaline conditions.^[18] However, it cannot be excluded that at neutral pH the Co(III)/Co(II) and the Co(IV)/Co(III) redox are shifted to higher potentials. This hypothesis could justify why no redox peak is present at neutral pH at ≈1.1 V_{RHE} and, then, the Co(III)/Co(II)

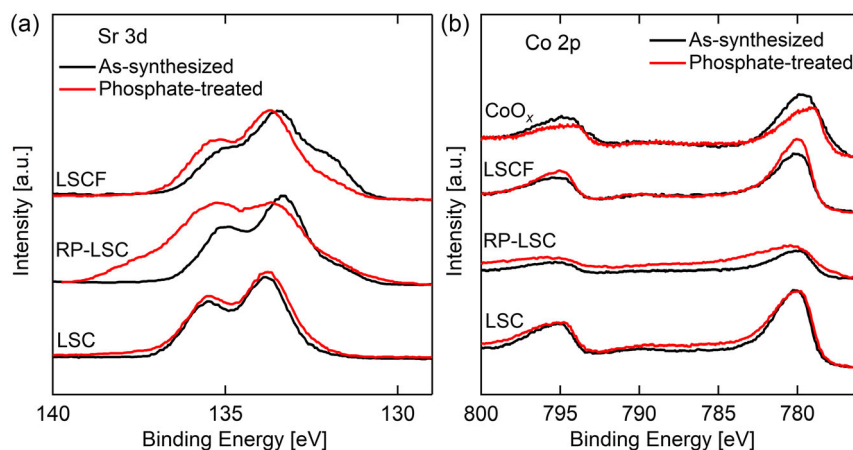


Figure 6. a) Sr 3d and b) Co 2p XPS core levels for all the investigated samples.

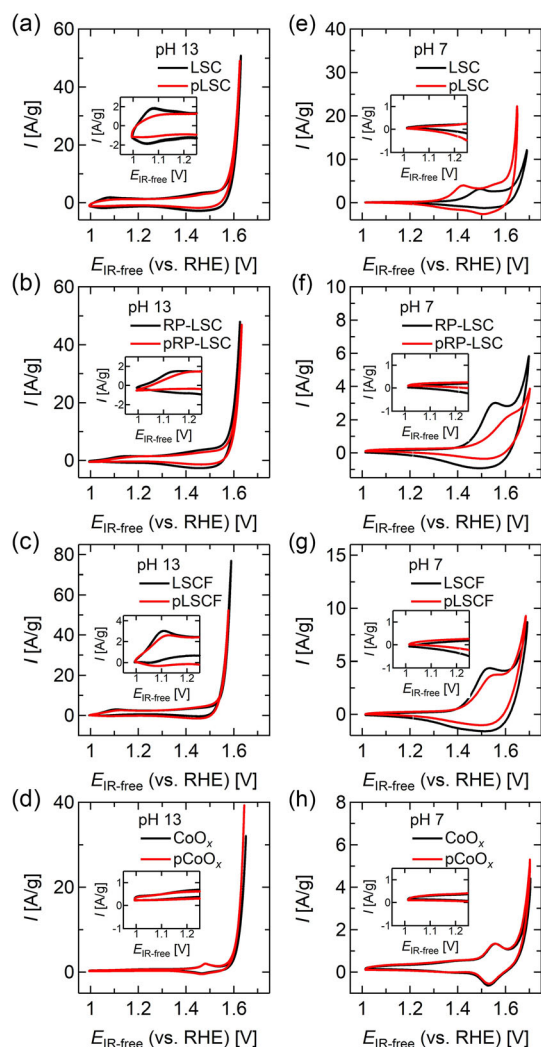


Figure 7. The cyclic voltammograms (25th cycle at 10 mV s^{-1}) of as-synthesized and phosphate-treated catalysts at a–d) pH 13 and e–h) pH 7 in a synthetic air-saturated electrolyte at the rotation speed of 900 rpm.

redox couple would first appear at $\approx 1.4\text{--}1.6 \text{ V}_{\text{RHE}}$. If shifted to higher potential in the neutral pH environment, the Co(IV)/Co(III) redox would not be visible in the CV because occurring within the OER region (where the OER current is much higher than the current associated to the redox). In addition, comparing the CVs at pH 7 for the as-synthesized and P-functionalized samples, the cobalt redox couple at $\approx 1.4\text{--}1.6 \text{ V}_{\text{RHE}}$ shifted toward the lower potential for P-treated LSC, while those of LSCF and RP-LSC shifted toward higher potential after phosphate treatment; CoO_x and pCoO_x showed very similar CVs, even though the largest amount of P was incorporated on the surface of pCoO_x according to ICP-OES measurements. The differences in the redox couple between pH 13 and pH 7, as well as between as-synthesized and P-treated samples, highlight a change in the redox chemistry on the catalyst surfaces. Focusing on the OER region of the CVs, it is interesting to note that, except for RP-LSC, phosphate-treated catalysts showed higher OER currents at neutral pH than as-synthesized catalysts, especially the LSC sample.

Table 1. Summary of electrochemical studies of the OER activity for the different perovskites studied: Tafel slope b , apparent mass-specific exchange current density j_0 , activity expressed as the mass-specific current density j at $1.58 \text{ V}_{\text{RHE}}$.

| pH | | LSC | pLSC | RP-LSC | pRP-LSC | LSCF | pLSCF | CoO_x | pCoO_x |
|------|---|-------|-------|--------|---------|--------|-------|----------------|-----------------|
| 7 | b [mV dec^{-1}] | 77 | 52 | 88 | 109 | 108 | 106 | 87 | 82 |
| | j_0 [A g^{-1}] | 1.61 | 1.59 | 1.64 | 1.65 | 1.63 | 1.63 | 1.66 | 1.66 |
| | $j_{@1.58 \text{ V}}$ [A g^{-1}] | 0.40 | 0.81 | 0.28 | 0.27 | 0.39 | 0.62 | 0.13 | 0.16 |
| 12.5 | b [mV dec^{-1}] | 69 | 55 | 59 | 61 | 35 | 38 | 62 | 55 |
| | j_0 [A g^{-1}] | 1.54 | 1.56 | 1.56 | 1.56 | 1.54 | 1.54 | 1.59 | 1.58 |
| | $j_{@1.58 \text{ V}}$ [A g^{-1}] | 3.55 | 2.70 | 1.9 | 2.18 | 20.18 | 15.89 | 0.69 | 0.96 |
| 13 | b [mV dec^{-1}] | 51 | 54 | 50 | 53 | 37 | 42 | 46 | 44 |
| | j_0 [A g^{-1}] | 1.54 | 1.54 | 1.54 | 1.54 | 1.50 | 1.50 | 1.58 | 1.57 |
| | $j_{@1.58 \text{ V}}$ [A g^{-1}] | 6.02 | 6.26 | 6.5 | 5.76 | 78.38 | 59.17 | 2.02 | 1.92 |
| 13.5 | b [mV dec^{-1}] | 42 | 55 | 61 | 59 | 30 | 46 | 46 | 44 |
| | j_0 [A g^{-1}] | 1.53 | 1.52 | 1.52 | 1.52 | 1.50 | 1.49 | 1.57 | 1.56 |
| | $j_{@1.58 \text{ V}}$ [A g^{-1}] | 18.84 | 15.73 | 10.61 | 11.35 | 233.04 | 88.92 | 3.47 | 3.86 |

The OER activity at different pHs was investigated to unveil the effect of phosphate treatment on the OER at different pHs. Table 1 and Figure 8 summarize the pH dependence of the mass normalized current density (A g^{-1}) at $1.58 \text{ V}_{\text{RHE}}$, Tafel slope, and apparent mass-specific exchange current density for each catalyst. In addition, Figure S6, Supporting Information, displays the CVs after 25 reverse scans for each catalyst at pH 12.5 and 13.5 and Figure S7, Supporting Information, provides Tafel plots at different pHs for each catalyst. Figure 8a–d shows a linear decrease of the mass activity in all catalysts in the pH ranges from 12.5 to 13.5. The slopes of the mass activity at $1.58 \text{ V}_{\text{RHE}}$ versus the pH values are reported in Table 2. LSC and LSCF revealed slopes close to unity in alkaline pH, in agreement with our previous study on ABO_3 single perovskites.^[12b] RP-LSC and binary cobalt oxide CoO_x had a fractional slope. A previous study pointed out that competing active sites lead to a fractional reaction order of activity vs pHs, as in the case of Co_3O_4 spinel with tetrahedral and octahedral sites.^[12c] A_2BO_4 RP-type perovskites exhibit strong anisotropic features with two types of oxygen species in the BO_6 octahedra, which are referred to as “apical” and “equatorial” oxygen sites. These distinct active oxygen sites might lead to a fractional reaction order, as observed in the present study for RP-LSC. Phosphate-treated LSC and LSCF catalysts showed a decreased slope of OER activity versus pHs, while similar slopes were observed for as-synthesized and P-treated CoO_x . Differently, pRP-LSC had a higher slope compared to RP-LSC. The slope can be correlated to the extent of the proton transfer in the LOER reaction. Referring to the LOER mechanism sketched in Figure 1, it is believed that the rate-determining step is the deprotonation step from $-\text{O}(\text{OH})$ layer to create the $-\text{O}(\text{O}^*)$ layer,^[10c] which would depend on the OH^- concentration and cause a degradation of the OER activity at near-neutral pHs. Thus, even though a decrease in LOER activity is expected decreasing pH, the lower the slope of the activity versus pH, the most performing is the catalyst at near neutral pHs as it

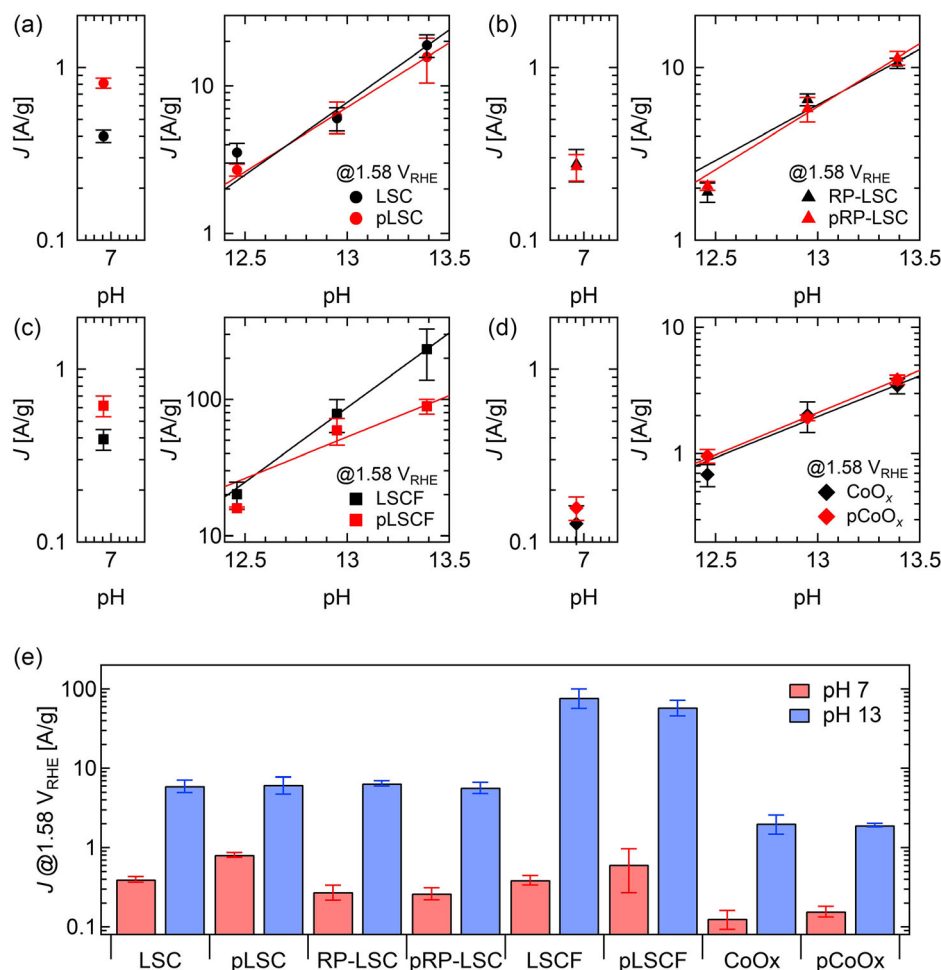


Figure 8. a–d) Mass activity at 1.58 V_{RHE} for each catalyst. Error bars were assigned using the standard deviation of the mass activities, which were determined from three repeated experiments. Actual measured pH values of electrolytes were plotted. e) Replot of mass activity at 1.58 V_{RHE} for each catalyst at pH 7 and pH 13.

Table 2. Slopes of $\delta \log(J)$ versus δpH in Figure 8a–d.

| | LSC | RP-LSC | LSCF | CoO _x |
|-------------------|-------------|-------------|-------------|------------------|
| As-synthesized | 1.00 ± 0.20 | 0.60 ± 0.20 | 1.09 ± 0.03 | 0.65 ± 0.09 |
| Phosphate-treated | 0.87 ± 0.05 | 0.73 ± 0.07 | 0.60 ± 0.20 | 0.67 ± 0.05 |

is in the present study pLSC. Figure 8e summarizes the catalyst mass activity at pH 13 and 7. While the OER activity is barely different for the as-synthesized and P-treated samples at pH 13, significant differences can be observed at pH 7, suggesting a significant role of the P-treatment on the OER mechanism at neutral pH. In particular, the increase in OER activity at pH 7 after the P-treatment follows the order: LSC > LSCF > CoO_x, while almost the same OER activity has been observed for RP-LSC after the P-treatment. The OER activity trend does not correlate with the amount of P incorporated on the surface of the catalysts, being pCoO_x the catalyst with the largest P content. The enhanced OER activity at pH 7 for P-treated LSC, LSCF, and CoO_x could originate from the ability of superficial

phosphate ion groups to assist the deprotonation step of the LOER mechanism when the OH[−] concentration in the electrolyte is low. It is worth noting that the phosphate treatment did not improve the OER activity at neutral pH in RP-LSC. XPS experiments revealed that RP-LSC has a large amount of electrochemically inert Sr-based surface segregated secondary phases compared to other cobalt-based catalysts, increasing largely after the P-treatment. This inert layer likely neutralizes the benefits gained by the phosphate ion functionalization, resulting in any OER activity enhancement at near-neutral pHs after the phosphate functionalization. The establishment of surface engineering to remove surface segregation toward an effective surface catalyst functionalization is a necessary step toward the development of OER catalysts for a wide range of electrolyte pHs. It must be also mentioned that hard and soft XAS measurements showed that LSC and RP-LSC had slightly reduced Co valence state after the P-treatment. Considering that RP-LSC suffers from surface segregations, which might hinder OER activity improvement after the P-treatment, another reason for the enhanced OER activity of P-treated LSC could be the

reduced Co oxidation state. In addition, LSCF, with an almost unchanged Co oxidation state after the P-treatment, displayed better OER activity at pH 7, but in less extent compared to LSC. Thus, it is likely that both the presence of phosphate ions on the catalyst surface and the reduced Co oxidation state can contribute to an enhanced OER activity at near-neutral pHs. Overall, the P-treatment is an appealing process to improve the current catalyst OER performance at near-neutral pHs, but more extensive investigations are needed to decouple the effect of the P-treatment on the catalyst electronic and local structure from the role of phosphate ion groups in the (L)OER mechanism and kinetics.

3. Conclusion

This study has investigated a dry phosphate ion treatment to functionalize nanosized cobalt-based OER catalysts ($\text{La}_{0.2}\text{Sr}_{0.8}\text{CoO}_{3-\delta}$, $\text{La}_{0.2}\text{Sr}_{0.8}\text{Co}_{0.8}\text{Fe}_{0.2}\text{O}_{3-\delta}$, $\text{La}_{0.5}\text{Sr}_{1.5}\text{CoO}_{4-\delta}$, and CoO_x) at near-neutral pHs. We proved that a dry treatment process using $\text{NaH}_2\text{PO}_2 \cdot \text{H}_2\text{O}$ as P source is effective for catalyst surface functionalization, especially for nanosized catalysts. Electrochemical evaluations revealed that phosphate ion-functionalized cobalt-based oxides, except for $\text{La}_{0.5}\text{Sr}_{1.5}\text{CoO}_{4-\delta}$, exhibited higher OER activity at neutral pH than the as-synthesized catalysts. The mechanism of deteriorated OER performance in $\text{La}_{0.5}\text{Sr}_{1.5}\text{CoO}_{4-\delta}$ at neutral pH was successfully explained by surface-sensitive soft XAS and XPS measurements. Electrochemically inert SrO-based surface segregations likely inhibit the phosphate ion functionalization on the active cobalt layer of $\text{La}_{0.5}\text{Sr}_{1.5}\text{CoO}_{4-\delta}$ and reduce OER activity, especially at near-neutral pHs. Differently, phosphate functionalization seems to be beneficial for CoO_x , $\text{La}_{0.2}\text{Sr}_{0.8}\text{CoO}_{3-\delta}$, and $\text{La}_{0.2}\text{Sr}_{0.8}\text{Co}_{0.8}\text{Fe}_{0.2}\text{O}_{3-\delta}$, and particularly for the $\text{La}_{0.2}\text{Sr}_{0.8}\text{CoO}_{3-\delta}$ catalyst. It is hypothesized that phosphate ion groups could assist the deprotonation step of the LOER mechanism in electrolytes with low OH^- concentration. In addition, we unveiled that P-treatment led to a reduced cobalt oxidation state in $\text{La}_{0.2}\text{Sr}_{0.8}\text{CoO}_{3-\delta}$, which could also boost its OER activity at neutral pH. Thus, it would be important in the future to decouple the effect of phosphate functionalization on the physicochemical properties of the catalysts from the phosphate ion role in the OER mechanism and kinetics. Additionally, optimization of the P-functionalization process could result in a further improvement of OER activity at neutral pH.

4. Experimental Section

Material Synthesis: LSC, LSCF, RP-LSC, and CoO_x have been synthesized by the flame spray synthesis setup.^[8h] Lanthanum nitrate hydrate ($\text{La}(\text{NO}_3)_3 \cdot x\text{H}_2\text{O}$, ≥ 99.9 Sigma-Aldrich, Switzerland), strontium nitrate ($\text{Sr}(\text{NO}_3)_2$, $\geq 98\%$, Sigma-Aldrich, Switzerland), cobalt nitrate hexahydrate ($\text{Co}(\text{NO}_3)_2 \cdot 6\text{H}_2\text{O}$, 99.9%, Sigma-Aldrich, Switzerland), and iron nitrate nonahydrate ($\text{Fe}(\text{NO}_3)_3 \cdot 9\text{H}_2\text{O}$, $\geq 98\%$, Sigma-Aldrich, Switzerland) were used as precursors. Precursors for each catalyst were added into a mixture of *N,N*-dimethylformamide (DMF, $\geq 99.8\%$, Switzerland), acetic acid (HAc, $\geq 99.0\%$, Sigma-Aldrich, Germany), and ultrapure water (MicroPure UV, Thermo Fisher Scientific, Reinach, Switzerland). The final solvent composition was DMF/HAc/ H_2O = 50/20/30 in volume. The total metal concentration in the precursor solution was 0.1 M for LSC, LSCF, RP-LSC, and 0.6 M for CoO_x , respectively.

For all catalysts, the precursor solutions were fed to the flame using a three-piston pump (C-601, Büchi, Switzerland) with a flow controller (C-610, Büchi, Switzerland) and a constant flow of 20 mL min^{-1} . The burner of the flame synthesis setup is block nozzle of a commercial flame cutter (Type 150–200, PanGas, Switzerland). In the center of the nozzle, a capillary (\varnothing inner = 1.05 mm, \varnothing outer = 1.6 mm) is located for injection of the liquid precursors. The dispersion gas is supplied through a circular gap (\varnothing = 3 mm) in the nozzle that is surrounding the capillary. Pure oxygen (99.95%, Pangas, Switzerland) was used as dispersion gas with a flow rate of 35 L min^{-1} for all catalysts. The combustion gas was formed by acetylene (99.6%, Pangas, Switzerland) and pure oxygen with a flow rate of 13 and 17 L min^{-1} , respectively. Finally, nanoparticle samples were collected on four ashless paper filters (Whatman, Sigma-Aldrich) using a bypass inlet with two vacuum pumps (VACFOX VC 50, Rietschle Thomas, Schopfheim, Germany).

For phosphate ion functionalization on the nanosized catalysts, wet and dry treatments were conducted, respectively. In both processes, $0.5 \text{ M K}_2\text{HPO}_4/\text{KH}_2\text{PO}_4$ buffer solution (pH 7)^[15] and $\text{NaH}_2\text{PO}_2 \cdot \text{H}_2\text{O}$ ^[8i,19] were used as the P source, respectively. In the former process, 100 mL of the buffer solution was prepared and then dispersed 500 mg of as-synthesized catalyst powders (only LSC performed in this study) into the buffer solution. After stirring at room temperature for 1 h, the powder samples were collected by filtration and washed with an excess amount of ultrapure water. After drying at room temperature overnight, the powder samples were further annealed at 350°C for 1 h under Ar gas flow. In the latter process, a crucible boat containing 100 mg of $\text{NaH}_2\text{PO}_2 \cdot \text{H}_2\text{O}$ and 50 mg of each catalyst was placed in the upstream and downstream positions in a tube furnace, respectively. Subsequently, the crucible boat was annealed at 300°C for 1 h with a heating speed of 3°C min^{-1} under Ar gas flow. The powder samples were finally obtained by natural cooling to room temperature.

Material Characterizations: The powder samples were characterized by powder XRD (SmartLab, Rigaku, Tokyo, Japan) with Cu K α polychromatic radiation (λ = 0.15418 nm) in a Bragg–Brentano geometry. The X-ray beam source was operated at 40 kV and 160 mA. The powder samples were placed on a Si-zero-background holder for each measurement. Diffraction patterns were collected with a diffractometer between 2θ = 5° and 90° , with a step of 0.01° , equipped with a Cu K β filter.

ICP-OES (Agilent 5100/5110 VDV) was used to quantify the amount of P in the treated samples (S2, Supporting Information). The ICP-OES samples were prepared using the following procedure: the powders were added into a mixture consisting of concentrated sub-boiled HNO_3 , HF (analytical grade purity), and ultrapure water (1:2:10); subsequently, transferred to a microwave reactor (turboWave easyCONTROL T660 cryoLAB 1000) to digest for 1 h at 270°C and 120 bar. After the systems cooled down, the resulting transparent solutions were diluted with ultrapure water before being subjected to ICP-OES analyses.

XPS measurements were performed with a VG ESCALAB 220iXL spectrometer (Thermo Fisher Scientific) with a base pressure of $\approx 2 \times 10^{-9}$ mbar using a focused monochromatized Al K α radiation (1486.6 eV) with a beam size of $\approx 500 \mu\text{m}^2$. The spectrometer was precalibrated by performing a measurement on a clean silver surface, whereby the Ag $3d_{5/2}$ peak was aligned to the binding energy of 368.25 eV with a full width at half maximum (FWHM) of 0.78 eV at pass energy of 30 eV. All survey spectra were recorded with a dwell time of 50 ms, using a pass energy of 50 eV in steps of 0.5 eV. For spectra acquired in a narrow energy scan, spectra were acquired with the pass energy of 30 eV in steps of 0.05 eV. The binding energy scale is calibrated using carbon C 1s peak (C–C binding energy of 284.5 eV).

Hard XAS measurements at the Co K-edge (7709 eV) and Fe K-edge (7112 eV) were performed at the SuperXAS beamline of the Swiss Light Source (PSI, Villigen, Switzerland) using the QEXAFS setup. A 2.9 T super-bend magnet source provided the beamline with a polychromatic photon beam. This beam was then collimated using a Si-coated mirror at 2.9 mrad followed by a LN cooled channel-cut Si(111) crystal monochromator. Finally, the beam was focused to a spot size of 1 by 0.2 mm using a Rh-coated toroidal mirror. All spectra were collected in transmission mode—a linear geometry—by using three 15 cm-long ionization

chambers filled with 1 bar of N₂ as detectors. Each sample was placed between the first and second chamber with simultaneous acquisition of the Co metal reference foil between the second and third chamber. The same procedure was repeated for measuring standards of cobalt(II) oxide (CoO, 99.99%, Sigma-Aldrich, Buchs, Switzerland) and lanthanum cobalt(III) oxide LaCoO₃ (LCO) to assign the Co oxidation state of the measured samples. Additionally, a 0.005 mm-thin Co metal foil (99.9%, GoodFellow, Huntingdon, UK) was used as a reference to calibrate the energy for all measurements by setting the first maximum of the first derivative of this Co K-edge spectrum to 7709 eV. Both K-edges (Co and Fe) were measured within one scan for all samples. This QEXAFS setup at the beamline allowed the collection of around 600 spectra and averaged together in a data acquisition time of 5 min per sample. The data processing was performed with ProQEXAFS.^[20]

Soft XAS measurements at the Co L-edge were carried out at the PHOENIX (PHotons for the Exploration of Nature by Imaging and XAFS) beamline of the Swiss Light Source. We used the soft X-ray branch line PHOENIX II with a planar grating monochromator covering energies from 0.3–2 keV. All experiments were performed in a vacuum chamber (10^{−5}–10^{−6} mbar) in total electron yield mode.

Electrochemical Characterizations: The electrocatalytic OER activity of all samples was tested in a three-electrode setup using a rotating disc electrode (RDE). This setup includes a multichannel potentiostat (VMP-300, BioLogic Science Instruments) with impedance spectroscopy capability, a modulated speed rotator (MSR, Pine Research Instrumentation, Durham, NC, USA), and a homemade cell out of a halved Nalgene fluorinated ethylene propylene (FEP) bottle (500 mL, Nalge Nunc International, Rochester, NY, USA) covered with a Teflon cap. The cell was half-filled with a freshly prepared potassium hydroxide solution (KOH, 99.99%, Sigma-Aldrich, Switzerland and ultrapure water (18.2 MΩ cm (Type I+/-), PURELAB Chorus1, Elga Veolia, High Wycombe, UK)) saturated with synthetic air (PanGas AG, Dagmersellen, Switzerland). 0.1 M KOH electrolyte was used as an internal solution for the Hg/HgO (RE-61AP, ALS, Tokyo, Japan) reference electrode. KOH pellets (Sigma-Aldrich, 99.99%) were dissolved in ultrapure water to prepare KOH electrolytes at appropriate concentrations corresponding to pHs (=12.5, 13.0, and 13.5), respectively, following the equation: pH = 14 − (−logC_{KOH}), where C_{KOH} [M] represents KOH concentration. We used 0.1 M KH₂PO₄/K₂HPO₄ as an electrolyte for pH 7. KH₂PO₄ and K₂HPO₄ were dissolved in ultrapure water to make the phosphate buffer solution. The actual pH value of each electrolyte was measured using a digital pH meter (913 pH meter, Metrohm AG, Switzerland). All specified potentials in this study were given concerning the reversible hydrogen electrode (RHE) scale indicated with the unit V_{RHE}. The potential difference between these two scales was determined with the calibration of the used reference electrode against a polycrystalline platinum disc (5.0 mm OD (0.196 cm²), Pine Research Instrumentation, Durham, NC, USA) immersed in the hydrogen-saturated electrolyte.

All electrochemical measurements were performed at room temperature, with a freshly flame-annealed gold mesh (Gold WOVEN Mesh/Gauze, Advent Research Materials Ltd., Oxford, UK) as a counter electrode and an RDE speed rate of 900 rpm. The working electrode was prepared by drop-casting 10 μL (5 μL twice) of an electrocatalyst containing suspension (2.0 g L^{−1}) on a freshly polished (0.3 and 0.05 μm MicroPolish alumina solution used on different MicroCloths, Buehler, Lake Blu, IL, USA) glassy carbon disc insert (GC, SIGRADUR G, 5.0 mm OD (0.2 cm²), HTW GmbH, Thierhaupten, Germany). The electrodes were dried in the air yielding an electrocatalyst loading of 0.1 mg_{oxide} cm^{−2}. The catalyst ink was produced ultrasonically (30 min, Ultrasonic Cleaner, VWR, Radnor, PA, USA) dispersing 5 mg of catalysts in a solution mixture of 2 mL 2-Propanol (IPA, 99.9% (HPLC Plus), Sigma-Aldrich, Buchs, Switzerland), 0.5 mL ultrapure water (18.2 MΩ cm (Type I+/-), PURELAB Chorus 1, Elga Veolia, High Wycombe, UK) and 10 μL of Na⁺-exchanged Nafion (NaOH, 99.99% and Nafion perfluorinated resin solution, 5 wt% in lower aliphatic alcohols and water, contains 15–20% water, Sigma-Aldrich, Switzerland).

The electrochemical protocol for determining the OER activity for the different synthesized catalysts included cyclic voltammetry (CV) between

1.0 V_{RHE} and 1.7 V_{RHE} (25 times) at a scan rate of 10 mV s^{−1} to reach a fairly reproducible CVs followed by chronoamperometric (CA) measurements. The steady-state current at 15 potential steps between 1.3 V_{RHE} and 1.7 V_{RHE} was measured while holding each potential for 30 s. This steady-state current in the linear range was then plotted as a Tafel plot to determine the OER activity of catalysts. Three impedance spectroscopy measurements were performed during this protocol, one at 1.2 V_{RHE} before the CV and two at 1.2 V_{RHE} and 1.4 V_{RHE} after the CA measurements to determine the ionic resistance of the setup, which was between 50 and 150 ohm (at low pH). Therefore, all applied potentials were corrected by the ohmic drop indicated in this study as E_{IR-free}. The current itself was normalized by the total mass (g_{oxide} = 20 μg) of the samples used during the experiment and is indicated as J. Each measurement was repeated at least 3 times using freshly prepared electrocatalyst containing suspensions.

Supporting Information

Supporting Information is available from the Wiley Online Library or from the author.

Acknowledgements

The authors acknowledge the financial contribution from the Swiss National Science Foundation with the SNSF PRIMA grant (PR00P2_193111). The authors would like to thank Mr. Dino Aegerter for the help and valuable comments on XAS and electrochemical characterizations.

Conflict of Interest

The authors declare no conflict of interest.

Data Availability Statement

The data that support the findings of this study are openly available in Materials Cloud at <https://doi.org/10.24435/materialscloud:gh-w0>, reference number 1022435.

Keywords

alkaline water electrolysis, cobalt-based oxide, neutral pH, oxygen evolution reaction, phosphate ion functionalization, surface segregation

Received: July 21, 2023

Published online:

- [1] a) K. Kodama, T. Nagai, A. Kuwaki, R. Jinnouchi, Y. Morimoto, *Nat. Nanotechnol.* **2021**, *16*, 140; b) S. E. Hosseini, B. Butler, *Int. J. Green Energy* **2020**, *17*, 13.
- [2] a) E. Fabbri, T. J. Schmidt, *ACS Catal.* **2018**, *8*, 9765; b) E. C. Beall, E. Fabbri, T. J. Schmidt, *ACS Catal.* **2021**, *11*, 3094; c) D. Hua, J. Huang, E. Fabbri, M. Rafique, B. Song, *ChemElectroChem* **2023**, *10*, e202200999; d) X. Xie, L. Du, L. Yan, S. Park, Y. Qiu, J. Sokolowski, W. Wang, Y. Shao, *Adv. Funct. Mater.* **2022**, *32*, 2110036.
- [3] a) X. Cheng, E. Fabbri, Y. Yamashita, I. E. Castelli, B.-J. Kim, M. Uchida, R. Haumont, I. Puente-Orench, T. J. Schmidt, *ACS Catal.* **2018**, *8*, 9567; b) I. Yamada, A. Takamatsu, K. Asai, T. Shirakawa, H. Ohzuku, A. Seno, T. Uchimura, H. Fujii,

- S. Kawaguchi, K. Wada, H. Ikeno, S. Yagi, *J. Phys. Chem. C* **2018**, *122*, 27885; c) B.-J. Kim, D. F. Abbott, X. Cheng, E. Fabbri, M. Nachttegaal, F. Bozza, I. E. Castelli, D. Lebedev, R. Schäublin, C. Copéret, T. Graule, N. Marzari, T. J. Schmidt, *ACS Catal.* **2017**, *7*, 3245; d) Y. Okazaki, Y. Fujita, H. Murata, N. Masuyama, Y. Nojima, H. Ikeno, S. Yagi, I. Yamada, *Chem. Mater.* **2022**, *34*, 10973.
- [4] a) A. Grimaud, K. J. May, C. E. Carlton, Y.-L. Lee, M. Risch, W. T. Hong, J. Zhou, Y. Shao-Horn, *Nat. Commun.* **2013**, *4*, 2439; b) B.-J. Kim, X. Cheng, D. F. Abbott, E. Fabbri, F. Bozza, T. Graule, I. E. Castelli, L. Wiles, N. Danilovic, K. E. Ayers, N. Marzari, T. J. Schmidt, *Adv. Funct. Mater.* **2018**, *28*, 1804355; c) E. Marelli, J. Gazquez, E. Poghossyan, E. Müller, D. J. Gawryluk, E. Pomjakushina, D. Sheptyakov, C. Piamonteze, D. Aegerter, T. J. Schmidt, M. Medarde, E. Fabbri, *Angew. Chem. Int. Ed.* **2021**, *60*, 14609.
- [5] a) S. Yagi, I. Yamada, H. Tsukasaki, A. Seno, M. Murakami, H. Fujii, H. Chen, N. Umezawa, H. Abe, N. Nishiyama, S. Mori, *Nat. Commun.* **2015**, *6*, 8249; b) A. Takamatsu, I. Yamada, S. Yagi, H. Ikeno, *J. Phys. Chem. C* **2017**, *121*, 28403; c) I. Yamada, H. Fujii, A. Takamatsu, H. Ikeno, K. Wada, H. Tsukasaki, S. Kawaguchi, S. Mori, S. Yagi, *Adv. Mater.* **2017**, *29*, 1603004; d) I. Yamada, A. Takamatsu, K. Asai, H. Ohzuku, T. Shirakawa, T. Uchimura, S. Kawaguchi, H. Tsukasaki, S. Mori, K. Wada, H. Ikeno, S. Yagi, *ACS Appl. Energy Mater.* **2018**, *1*, 3711.
- [6] a) R. P. Forslund, W. G. Hardin, X. Rong, A. M. Abakumov, D. Filimonov, C. T. Alexander, J. T. Mefford, H. Iyer, A. M. Kolpak, K. P. Johnston, K. J. Stevenson, *Nat. Commun.* **2018**, *9*, 3150; b) S. Liu, H. Luo, Y. Li, Q. Liu, J.-L. Luo, *Nano Energy* **2017**, *40*, 115; c) Y. Zhu, H. A. Tahini, Z. Hu, Y. Yin, Q. Lin, H. Sun, Y. Zhong, Y. Chen, F. Zhang, H.-J. Lin, C.-T. Chen, W. Zhou, X. Zhang, S. C. Smith, Z. Shao, H. Wang, *EcoMat* **2020**, *2*, e12021; d) Y. Zhu, Q. Lin, Z. Hu, Y. Chen, Y. Yin, H. A. Tahini, H.-J. Lin, C.-T. Chen, X. Zhang, Z. Shao, H. Wang, *Small* **2020**, *16*, 2070108; e) M. Retuerto, L. Pascual, J. Torrero, M. A. Salam, Á. Tolosana-Moranchel, D. Gianolio, P. Ferrer, P. Kayser, V. Wilke, S. Stiber, V. Celorrio, M. Mokhtar, D. G. Sanchez, A. S. Gago, K. A. Friedrich, M. A. Peña, J. A. Alonso, S. Rojas, *Nat. Commun.* **2022**, *13*, 7935.
- [7] a) J. Kim, X. Yin, K.-C. Tsao, S. Fang, H. Yang, *J. Am. Chem. Soc.* **2014**, *136*, 14646; b) E. Tsuji, T. Motohashi, H. Noda, D. Kowalski, Y. Aoki, H. Tanida, J. Niikura, Y. Koyama, M. Mori, H. Arai, T. Ioroi, N. Fujiwara, Y. Uchimoto, Z. Ogumi, H. Habazaki, *ChemSusChem* **2017**, *10*, 2864; c) D. Kowalski, H. Kiuchi, T. Motohashi, Y. Aoki, H. Habazaki, *ACS Appl. Mater. Interfaces* **2019**, *11*, 28823.
- [8] a) J. Suntivich, K. J. May, H. A. Gasteiger, J. B. Goodenough, Y. Shao-Horn, *Science* **2011**, *334*, 1383; b) E. Fabbri, M. Nachttegaal, X. Cheng, T. J. Schmidt, *Adv. Energy Mater.* **2015**, *5*, 1402033; c) J.-I. Jung, S. Park, M.-G. Kim, J. Cho, *Adv. Energy Mater.* **2015**, *5*, 1501560; d) X. Cheng, E. Fabbri, B. Kim, M. Nachttegaal, T. J. Schmidt, *J. Mater. Chem. A* **2017**, *5*, 13130; e) E. Fabbri, M. Nachttegaal, T. Binninger, X. Cheng, B.-J. Kim, J. Durst, F. Bozza, T. Graule, R. Schäublin, L. Wiles, M. Pertoso, N. Danilovic, K. E. Ayers, T. J. Schmidt, *Nat. Mater.* **2017**, *16*, 925; f) I. Yamada, T. Otake, K. Asai, K. Oka, S. Kawaguchi, K. Wada, S. Yagi, *Mater. Chem. Front.* **2019**, *3*, 1209; g) B.-J. Kim, E. Fabbri, D. F. Abbott, X. Cheng, A. H. Clark, M. Nachttegaal, M. Borlaf, I. E. Castelli, T. Graule, T. J. Schmidt, *J. Am. Chem. Soc.* **2019**, *141*, 5231; h) D. Aegerter, M. Borlaf, E. Fabbri, A. H. Clark, M. Nachttegaal, T. Graule, T. J. Schmidt, *Catalysts* **2020**, *10*, 984; i) Z. Zhang, W. Zhou, Z. Yang, J. Jiang, D. Chen, Z. Shao, *Int. J. Hydrogen Energy* **2020**, *45*, 24859; j) X. Cao, X. Yan, L. Ke, K. Zhao, N. Yan, *ACS Appl. Mater. Interfaces* **2021**, *13*, 22009.
- [9] a) G. Ou, C. Yang, Y. Liang, N. Hussain, B. Ge, K. Huang, Y. Xu, H. Wei, R. Zhang, H. Wu, *Small Methods* **2019**, *3*, 1800279; b) C. Zhao, N. Li, R. Zhang, Z. Zhu, J. Lin, K. Zhang, C. Zhao, *ACS Appl. Mater. Interfaces* **2019**, *11*, 47858; c) R. Q. Zong, Y. G. Fang, C. R. Zhu, X. Zhang, L. Wu, X. Hou, Y. K. Tao, J. Shao, *ACS Appl. Mater. Interfaces* **2021**, *13*, 42852.
- [10] a) T. Binninger, R. Mohamed, K. Waltar, E. Fabbri, P. Levecque, R. Kötz, T. J. Schmidt, *Sci. Rep.* **2015**, *5*, 12167; b) J. T. Mefford, X. Rong, A. M. Abakumov, W. G. Hardin, S. Dai, A. M. Kolpak, K. P. Johnston, K. J. Stevenson, *Nat. Commun.* **2016**, *7*, 11053; c) A. Grimaud, O. Diaz-Morales, B. Han, W. T. Hong, Y.-L. Lee, L. Giordano, K. A. Stoerzinger, M. T. M. Koper, Y. Shao-Horn, *Nat. Chem.* **2017**, *9*, 457; d) Y. Pan, X. Xu, Y. Zhong, L. Ge, Y. Chen, J.-P. M. Veder, D. Guan, R. O'Hayre, M. Li, G. Wang, H. Wang, W. Zhou, Z. Shao, *Nat. Commun.* **2020**, *11*, 2002.
- [11] P. P. Lopes, D. Y. Chung, X. Rui, H. Zheng, H. He, P. F. B. D. Martins, D. Strmcnik, V. R. Stamenkovic, P. Zapol, J. F. Mitchell, R. F. Klie, N. M. Markovic, *J. Am. Chem. Soc.* **2021**, *143*, 2741.
- [12] a) B. Han, M. Risch, Y.-L. Lee, C. Ling, H. Jia, Y. Shao-Horn, *Phys. Chem. Chem. Phys.* **2015**, *17*, 22576; b) B.-J. Kim, E. Fabbri, M. Borlaf, D. F. Abbott, I. E. Castelli, M. Nachttegaal, T. Graule, T. J. Schmidt, *Mater. Adv.* **2021**, *2*, 345; c) L. Giordano, B. Han, M. Risch, W. T. Hong, R. R. Rao, K. A. Stoerzinger, Y. Shao-Horn, *Catal. Today* **2016**, *262*, 2.
- [13] a) J. Durst, A. Rudnev, A. Dutta, Y. Fu, J. Herranz, V. Kaliginedi, A. Kuzume, A. A. Permyakova, Y. Paratcha, P. Broekmann, T. J. Schmidt, *Chimia* **2015**, *69*, 769; b) J. Herranz, J. Durst, E. Fabbri, A. Pătru, X. Cheng, A. A. Permyakova, T. J. Schmidt, *Nano Energy* **2016**, *29*, 4.
- [14] J. Herranz, A. Pătru, E. Fabbri, T. J. Schmidt, *Curr. Opin. Electrochem.* **2020**, *23*, 89.
- [15] C. Yang, C. Laberty-Robert, D. Batuk, G. Cibir, A. V. Chadwick, V. Pimenta, W. Yin, L. Zhang, J.-M. Tarascon, A. Grimaud, *J. Phys. Chem. Lett.* **2017**, *8*, 3466.
- [16] K. Momma, F. Izumi, *J. Appl. Crystallogr.* **2011**, *44*, 1272.
- [17] a) A. Boucly, E. Fabbri, L. Artiglia, X. Cheng, D. Pergolesi, M. Ammann, T. J. Schmidt, *Chem. Mater.* **2020**, *32*, 5256; b) Z. Cai, M. Kubicek, J. Fleig, B. Yildiz, *Chem. Mater.* **2012**, *24*, 1116; c) Y. Chen, H. Téllez, M. Burriel, F. Yang, N. Tsvetkov, Z. Cai, D. W. McComb, J. A. Kilner, B. Yildiz, *Chem. Mater.* **2015**, *27*, 5436.
- [18] A. Bergmann, E. Martinez-Moreno, D. Teschner, P. Chernev, M. Gliech, J. F. de Araujo, T. Reier, H. Dau, P. Strasser, *Nat. Commun.* **2015**, *6*, 8625.
- [19] a) T. Zhai, L. Wan, S. Sun, Q. Chen, J. Sun, Q. Xia, H. Xia, *Adv. Mater.* **2017**, *29*, 1604167; b) Z. Li, L. Lv, J. Wang, X. Ao, Y. Ruan, D. Zha, G. Hong, Q. Wu, Y. Lan, C. Wang, J. Jiang, M. Liu, *Nano Energy* **2018**, *47*, 199; c) Y. Li, C. Zhao, *ACS Catal.* **2017**, *7*, 2535; d) Z. Wang, H. Liu, R. Ge, X. Ren, J. Ren, D. Yang, L. Zhang, X. Sun, *ACS Catal.* **2018**, *8*, 2236.
- [20] A. H. Clark, J. Imbao, R. Frahm, M. Nachttegaal, *J. Synchrotron Radiat.* **2020**, *27*, 551.